PHILOSOPHICAL TRANSACTIONS OF THE ROYAL SOCIETY A

Phil. Trans. R. Soc. A (2008) **366**, 1275–1296
doi:10.1098/rsta.2007.2131
Published online 5 November 2007

Experiments on vertical slender flexible cylinders clamped at both ends and subjected to axial flow

By Y. Modarres-Sadeghi, M. P. Païdoussis*, C. Semler and E. Grinevich

Department of Mechanical Engineering, McGill University, 817 Sherbrooke Street West, Montreal, Quebec, Canada H3A 2K6

Three series of experiments were conducted on vertical clamped–clamped cylinders in order to observe experimentally the dynamical behaviour of the system, and the results are compared with theoretical predictions. In the first series of experiments, the downstream end of the clamped–clamped cylinder was free to slide axially, while in the second, the downstream end was fixed; the influence of externally applied axial compression was also studied in this series of experiments. The third series of experiments was similar to the second, except that a considerably more slender, hollow cylinder was used. In these experiments, the cylinder lost stability by divergence at a sufficiently high flow velocity and the amplitude of buckling increased thereafter. At higher flow velocities, the cylinder lost stability by flutter (attainable only in the third series of experiments), confirming experimentally the existence of a post-divergence oscillatory instability, which was previously predicted by both linear and nonlinear theory. Good quantitative agreement is obtained between theory and experiment for the amplitude of buckling, and for the critical flow velocities.

Keywords: flexible cylinders; axial flow; stability; nonlinear dynamics; post-divergence flutter; experiments

1. Introduction

The dynamical behaviour of cylinders supported at both ends and subjected to axial flow was studied very comprehensively using a linear theory by Païdoussis (1966*a*, 1973, 2004), supported also by experiments (Païdoussis 1966*b*). To analyse the system behaviour using the linear model, the dimensionless complex frequencies for the cylinder were plotted in Argand diagrams with the dimensionless flow velocity as the independent parameter (Païdoussis 1973). It was shown that, for small flow velocities, the free motion of the cylinder is damped. However, for sufficiently high flow velocities, the first mode frequency becomes purely imaginary corresponding to the onset of divergence, followed by divergence in the second mode. At slightly

* Author for correspondence (michael.paidoussis@mcgill.ca; mary.fiorilli@mcgill.ca).

Electronic supplementary material is available at http://dx.doi.org/10.1098/rsta.2007.2131 or via http://www.journals.royalsoc.ac.uk.

One contribution of 6 to a Theme Issue 'Experimental nonlinear dynamics II. Fluids'.

higher flow velocity, the negative branches of the first- and second-mode loci coalesce and leave the imaginary-frequency axis at a point where the damping is negative, indicating the onset of coupled-mode flutter. The interested reader is also referred to the work of Chen & Wambsganss (1972); see also Chen (1987).

For a cantilevered cylinder with a fairly well-streamlined free end, it was shown that the cylinder loses stability by divergence in its first mode, but, as the flow velocity is increased further, it regains stability (Païdoussis 1966*a*, 1973); subsequently, it loses stability by single- or coupled-mode flutter, depending on the system parameters. At higher flow velocities, the cylinder loses stability in the third mode. Further work was done on pinned–free cylinders and strings in axial flow by Triantafyllou & Chryssostomidis (1984, 1985). In addition, some closely related work on towed cylinders in axial flow is of interest (Païdoussis 1968; Ortloff & Ives 1969; Pao 1970; Lee 1981; Kennedy 1987; Dowling 1988*a*,*b*).

Païdoussis (1966*b*) conducted a series of experiments to study the dynamical behaviour of flexible cylinders in axial flow and to measure the limits of stability, and compared them with the theoretical results found using the linear model. In experiments with clamped–free cylinders, a thin metal strip was embedded in the cylinder along its length, in the vertical plane of symmetry, effectively limiting all motion to the horizontal plane and also providing additional support in the vertical plane in cases where the weight of the cylinder was considerably greater, or smaller, than that of the displaced water. Cylinders with both ends supported were not fitted with a metal strip, so that the development of instability would not be impeded by excessive resistance to axial extension.

In all the tests, at small flow velocities, small random vibrations were damped. For cantilevered cylinders, tapered at the free end, the system became unstable at sufficiently high flow velocity. The system first buckled and then, as the flow velocity was increased, it developed second-mode oscillation (flutter), followed by third-mode oscillation. Similar observations were made with a cylinder pinned at the upstream end and free at the other end.

For a very long simply supported cylinder, it was observed that it sagged slightly at its midpoint under its own weight. Increasing the flow velocity in such cases exaggerated this sag and slowly shifted it to the horizontal plane, but no distinct threshold of buckling and no oscillatory motions were observed. For shorter cylinders, however, at a sufficiently high flow velocity, a small bow developed just downstream of the midpoint of the cylinder, increasing in amplitude with flow; thus the system lost stability by divergence (buckling). This was followed by a spontaneous second-mode oscillation.

Lopes *et al.* (2002) derived a nonlinear equation of motion to describe the dynamics of a slender cantilevered cylinder in axial flow, generally terminated by an ogival free end, using the inextensibility assumption, which is reasonable for cantilevered cylinders. Inviscid forces were modelled by an extension of Lighthill's slender-body theory to third-order accuracy. The viscous, hydrostatic and gravity-related terms were derived separately to the same accuracy. The equation of motion was obtained via Hamilton's principle. The boundary conditions related to the ogival free end were also derived separately.

Using this model, the nonlinear dynamics of the system was studied (Semler *et al.* 2002). It was found that the cylinder first loses stability by divergence in its first mode, the amplitude of which increases with flow. This is gradually transformed to divergence of predominantly second-mode shape, before the

system is restabilized. At slightly higher flow velocities, stability is lost by second-mode flutter, which at still higher flows is succeeded by third-mode flutter. No chaotic oscillation was observed in this study. One important result, obtained by examining the system from the nonlinear point of view, is that post-divergence flutter does materialize, as predicted by linear theory, whether there is post-divergence restabilization or not.

This theoretical work was also supported by an experimental study (Païdoussis *et al.* 2002) using a water tunnel with a vertical test section. The flexible cylinder was mounted vertically in the middle of the water tunnel, with no central metal strip embedded in it, as it was no longer essential (as it was in the earlier experiments with a horizontal cylinder). Initially, as the flow was increased, flow-induced damping was generated, but small vibration could be observed in which the cylinder responded to the turbulence-induced fluctuating pressure field. At higher flow velocities, the system developed divergence in its first mode and then regained its equilibrium configuration, before developing flutter spontaneously in its second mode. As the flow velocity continued to increase, second-mode flutter was succeeded by third-mode flutter, and in some cases fourth-mode flutter. This was the dynamical behaviour for a cylinder with a reasonably well-streamlined ogival end shape at the free end. If, however, the end was completely blunt, then neither static (divergence) nor dynamic (flutter) instabilities materialized; the reasons for this are elucidated in Païdoussis (2004, §8.3.3).

Later, a nonlinear model was derived for a cylinder with both ends supported subjected to axial flow (Modarres-Sadeghi *et al.* 2005). Using this nonlinear model, the behaviour of the system was studied for cylinders with various boundary conditions (Modarres-Sadeghi *et al.* 2007).

Much of the research work referred to in the foregoing was curiosity driven. However, the work on cylinders in axial flow was inspired by applications to heat exchanger and nuclear reactor internals (Chen 1987; Païdoussis 2004). Also, the work on towed cylinders was undertaken for application to the stability of (i) the Dracone barge (Hawthorne 1961), (ii) acoustic arrays used in underwater oil and gas exploration (Dowling 1988*a*,*b*; Poddubny *et al.* 1995; Sudarsan *et al.* 1997), and (iii) towed underwater pipelines (Sarv & John 2000). Other applications have also emerged, e.g. in fibre spinning and wire coating (Poddubny & Saltanov 1991; Papanastasiou *et al.* 2000), and for modelling the dynamics of high-speed trains in tunnels (Sugimoto 1996; Sugimoto & Kugo 2001; Tanaka *et al.* 2001).

The experimental behaviour of a vertical cylinder supported at both ends is discussed in this paper from a nonlinear point of view. According to the nonlinear theory cited above, as the flow velocity is increased, the cylinder buckles at a certain flow velocity and the amplitude of buckling increases thereafter. At higher flow, the statically deformed cylinder undergoes a Hopf bifurcation, which gives rise to periodic oscillations, followed by quasi-periodic and chaotic oscillations. The aim of the experiments to be described was (i) to measure again the critical flow velocities for divergence (buckling) and flutter, (ii) to observe the post-divergence behaviour of the system and measure the corresponding data (the amplitude of buckling, as well as the amplitude and the frequency of oscillations in the case of dynamic motions, if they materialize), and (iii) to compare the experimental observations with the predictions of nonlinear theory, both qualitatively and quantitatively, in order to validate the theoretical model, hopefully by observing experimentally the same sequence of dynamical states predicted by the nonlinear theory.

2. The nonlinear model, methods of solution and typical theoretical results

The weakly nonlinear equations of motion for a slender flexible cylinder of length L, diameter D and mass per unit length m, subjected to axial flow (with flow velocity U and added mass per unit length, in unconfined flow, M), have been derived by Modarres-Sadeghi *et al.* (2005) and are given in appendix A. In that derivation, the cylinder centreline is considered to be extensible, and hence two coupled nonlinear equations describe its motion, involving both longitudinal and transverse displacements. The fluid forces are formulated in terms of several components, for convenience. For high Reynolds number flows, the dominant inviscid component is modelled by an extension of Lighthill's slender-body work; frictional, hydrostatic and pressure-loss forces are then added to the inviscid component. The derivation of the equations of motion is carried out in a Lagrangian framework, and the resultant equations are correct to third order of magnitude, where the transverse displacement of the cylinder is of first order. The resulting nonlinear partial differential equations are then discretized using the Galerkin technique, leading to a set of second-order ordinary differential equations, which can be recast in first-order form. To solve this set of ordinary differential equations, two methods have been used: Houbolt's finite difference method (Semler *et al.* 1996) and Auto (Doedel & Kernéves 1986), which is a computational package based on continuation methods. For details on the derivation of the equations of motion and also the methods of solution, see Modarres-Sadeghi (2006).

In the equations of motion (see appendix A), ζ and η are, respectively, the non-dimensional displacements in the longitudinal and transverse direction; $\mathcal{U}$ is the dimensionless flow velocity, used extensively as the independent parameter in studying the dynamics of the system; β is a mass ratio; Π_0, $\bar{\Pi}$ and $\bar{\Gamma}$ are dimensionless measures of axial flexibility, pressurization and externally imposed uniform tension, respectively; c_n and c_t are the coefficients of frictional forces in the normal and tangential (longitudinal) direction, respectively; c_d is the coefficient of transverse form drag; $\delta = 0$ if the downstream end is free to slide axially (or wholly free), and $\delta = 1$ if it is axially fixed; ν is the Poisson ratio; γ is a gravity coefficient; c_b is the base-drag coefficient acting in the longitudinal direction at the downstream end of the cylinder when $\delta = 0$; ε is the slenderness ratio; $h = D/D_\mathrm{h}$ is a hydrodynamic confinement coefficient, D_h being the hydraulic diameter; and χ is an added mass coefficient which increases with increasing confinement.

Figure 1*a* shows a typical theoretical bifurcation diagram of the system of a clamped–clamped cylinder found by Auto, where q_1 (first generalized coordinate in the transverse direction, which is representative of the overall transverse displacement of the cylinder) is plotted versus non-dimensional flow velocity, $\mathcal{U}$. The cylinder is at its original equilibrium state at low flow velocities. With increasing flow, it loses stability via a supercritical pitchfork bifurcation at a non-dimensional flow velocity $\mathcal{U} \simeq 2\pi$ (BP in figure 1*a*) leading to divergence. The original equilibrium becomes unstable for $\mathcal{U} > 2\pi$; the dotted line on the horizontal axis corresponds to this unstable state. The amplitude of buckling (q_1) increases with the flow ($\mathcal{U}$). The static solution eventually loses stability, and the system develops flutter via a supercritical Hopf bifurcation at $\mathcal{U} = 21.60$ (HB in figure 1*b*) giving rise to periodic solutions. This oscillatory motion loses stability via a period-doubling bifurcation at $\mathcal{U} = 21.92$ and the system develops period-2

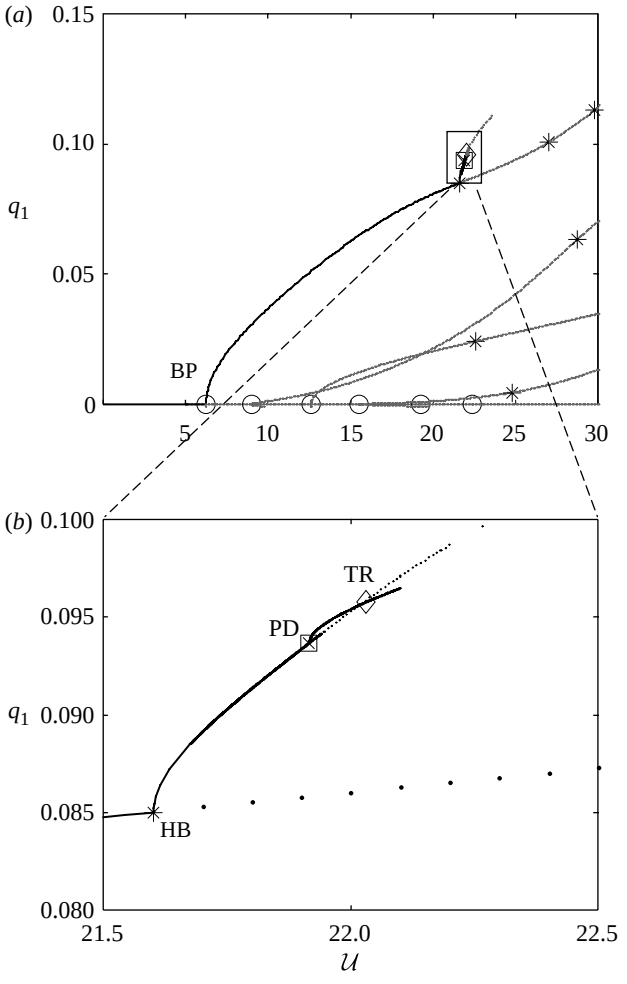

Figure 1. (*a*,*b*) A typical bifurcation diagram for a clamped–clamped cylinder.

motions afterward (PD in figure 1*b*). Quasi-periodic oscillations are observed for flow velocities greater than $\mathcal{U} = 22.03$ (TR in figure 1*b*), where a torus bifurcation occurs. The quasi-periodic oscillations become chaotic at $\mathcal{U} \simeq 23$ and remain chaotic thereafter for the flow range studied.

In the theoretical results presented in the following sections, the eigenfunctions of a clamped–clamped cylinder for the transverse deformation are used as basis functions for the transverse displacement. For the case of a clamped–sliding cylinder (§4), the eigenfunctions of a fixed–sliding bar undergoing axial vibration are used as basis functions for the axial displacement, reflecting the fact that axial displacement at the lower end of the cylinder can occur freely; however, for the case of a clamped–clamped cylinder with no end-sliding (§§5 and 6), the eigenfunctions of a bar with both ends fixed have been used. In the computations of §4, only two modes in each direction have been used to discretize the partial differential equation, because the maximum flow studied therein is not very high, and this was sufficient to obtain converged results; in contrast, at least six modes in each direction have been used in the computations of §§5 and 6. Six modes in

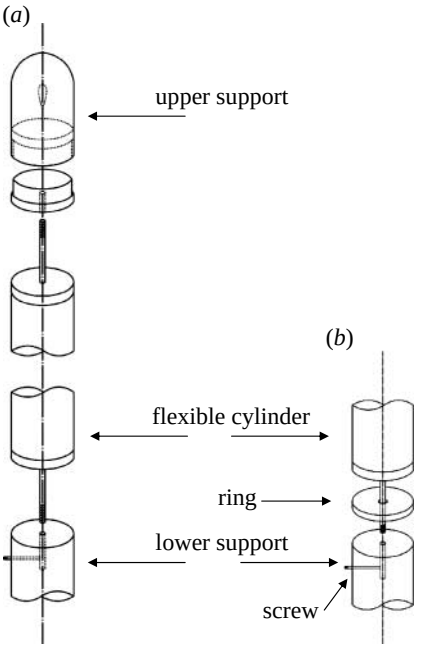

Figure 2. (*a*) A schematic, exploded view of the cylinder and its upstream and downstream ends and (*b*) a schematic view of the downstream end of the system with a ring inserted between the lower end of the cylinder and the lower support (second series of experiments).

each direction were also used in generating the bifurcation diagram of figure 1. An appropriate convergence study has been conducted for this purpose (Modarres-Sadeghi 2006).

3. Experimental set-up

The experiments were conducted with flexible cylinders, which were made of silicone rubber by casting in special moulds. Each cylinder was fitted at its two extremities with metal discs (of the same diameter as the cylinder), which could be screwed onto different support assemblies at the upper and lower ends to provide clamped boundary conditions (see figure 2*a*).[1] The upper support was well streamlined. The cylinder was mounted vertically in the test section of the water tunnel, which is shown schematically in figure 3. The test-section ('channel') diameter is $D_{\mathrm{ch}}=0.20$ m and its length is $L_{\mathrm{ch}}=0.75$ m. Flow straighteners, screens and a large flow-area reduction upstream were used to ensure a uniform axial flow-stream in the test section. The velocity profile is flat and uniform over the central portion of the test section, covering at least 15 cm in diameter. The highest attainable flow velocity in the water tunnel is 5 m s^{-1} (see Païdoussis (2004, ch. 8), for a complete description of the water tunnel).

To measure the midpoint displacement of the cylinder, two non-contacting optical motion-followers were used, measuring the displacement in two perpendicular directions to guarantee that the plane and the value of the

[1] For details about the method of making these cylinders, see Païdoussis (1998, appendix D).

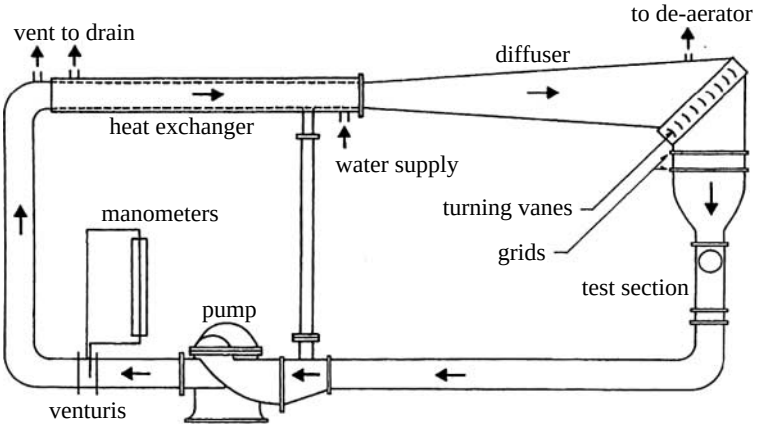

Figure 3. Schematic view of the water tunnel (adapted from Païdoussis *et al.* (2002)).

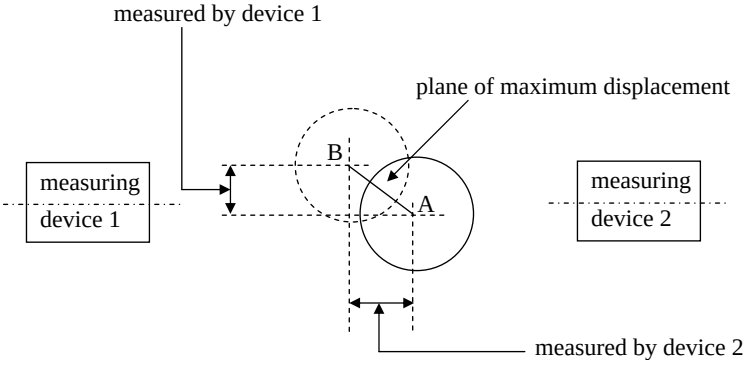

Figure 4. Schematic of the motion-followers ('measuring devices') set-up. Distance AB is the maximum measured displacement based on the measurements by the two devices.

maximum displacement were determined. Figure 4 shows schematically how the two motion-followers were placed relative to the cylinder. The first measuring device ('device 1') measured displacements of the cylinder perpendicular to the axis of the device, while the second measured those in the direction of its axis. The output of these two motion-followers was saved in a computer for later analysis by the LabView software. The resultant of these two measurements, as shown in figure 4, gives the plane and the value of the maximum displacement, which is the value that can be compared with the theoretical predictions.

In each experiment, the flow velocity was increased gradually from zero, and at each step the midpoint displacement of the cylinder was measured. The dimensional and dimensionless parameters for the cylinders used in the experiments are listed in tables 1 and 2.

First, experiments with a cylinder clamped at both ends, but free to slide axially at its downstream end are discussed (§4). Then, the results for clamped–clamped cylinders with no axial sliding are presented (§5); the influence of axial compression is also studied experimentally in this case. Because no dynamic instability was observed in these two series of experiments due to flow limitations of the water tunnel, another series was conducted in which a more flexible

Table 1. Physical parameters of the cylinders used in the three series of experiments.

physical parameter	series 1 and 2	series 3
outer cylinder diameter, D_o (mm)	25.4	15.6
inner cylinder diameter, D_i (mm)	0	9.4
length, L (mm)	520	435
mass per unit length, m (kg m^{-1})	0.577	0.1445
flexural rigidity, EI (N m^2)	0.0559	0.0065

Table 2. Dimensionless parameters used in the theoretical calculations for the three series of experiments, with cylinders the physical parameters of which are given table 1. (The non-dimensional parameters are defined in equation (A 3).)

series	Π_0	β	γ	ε	h	χ	c_d	c_t	c_n/c_t
1 and 2	6707	0.47	1.83	20.47	0.125	1.032	0.0	0.025	1
3	9124.2	0.57	−5.78	27.88	0.0768	1.0119	0.005	0.02	0.5

cylinder was used; these experiments, in which flutter *was* observed, are discussed in §6.

In all the experiments, graphs of the frequency versus non-dimensional flow velocity are presented for pre-buckling turbulence-induced vibrations of the cylinders. Also, in each case, bifurcation diagrams of the system are presented in which the maximum midpoint amplitude of the cylinder is plotted versus non-dimensional flow velocity. Different methods for the determination of the onset of divergence are discussed. The influence of different parameters on the onset of periodic motions is also discussed.

4. First series of experiments: clamped–sliding cylinder

In the first series of experiments, the lower end of the cylinder was free to slide axially in its support; the set screw at the lower support (figure 2) was not tightened. For the parameters of this cylinder and the maximum flow rate attainable in the water tunnel, the maximum non-dimensional flow velocity for this system was $\mathcal{U} = 7$.

At small flow velocities, turbulence-induced damped vibrations were observed about the stretched-straight equilibrium position of the cylinder. With increasing flow, the cylinder buckled, essentially in its first beam-mode shape, i.e. its deflection amplitude at the midpoint increased sharply. This, however, occurred at almost the maximum attainable flow; therefore, the cylinder behaviour substantially beyond the onset of divergence could not be observed. The PSD plots of the vibrations of the cylinder were produced at each flow velocity to construct the frequency versus flow graph and thus obtain the critical value for divergence (as discussed in the next paragraph). Figure 5 shows the PSDs of the vibrations of the cylinder measured at its midpoint at two different flow velocities before the onset of divergence. The dominant frequency of vibration is $f_1 = 3.5$ Hz

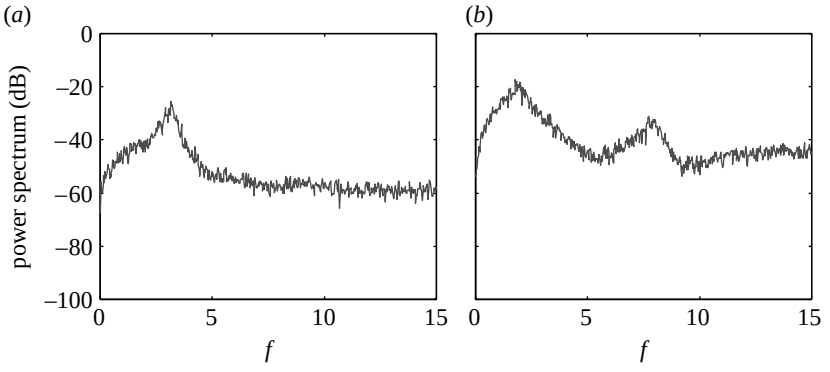

Figure 5. PSD plots for the first series of experiments with a clamped–sliding cylinder with parameters given in table 1 (series 1) at (*a*) $\mathcal{U} = 2.2$ and (*b*) $\mathcal{U} = 5.6$.

for $\mathcal{U} = 2.2$ (figure 5*a*), which can be identified with the first eigenfrequency of the system at this flow. At $\mathcal{U} = 5.6$, two peaks are noticeable in the PSD plot: $f_1 = 2$ Hz and $f_2 = 8$ Hz, which correspond, respectively, to the first and the second eigenfrequency of the system.[2] It is observed that the eigenfrequencies of the system vary with the flow velocity.

Figure 6*a* shows how the dominant frequency ($\omega_1 = 2\pi f_1$) varies with the non-dimensional flow velocity for this system. The asterisks are the experimental results and the dots are the theoretical ones. Theoretically, the first-mode frequency varies with $\mathcal{U}$ quasi-parabolically, and at the onset of divergence the first-mode frequency vanishes: $\omega_1 = 0$. The experimental values follow very closely the theoretical parabola, showing good agreement between theory and experiment. To approximate the critical flow velocity for divergence, one should fit a parabola to the experimental results (the continuous line in figure 6*a*) and extend it to cross the flow-velocity axis at a point which may be considered as the critical flow velocity for divergence. This is called 'the first method' for determining the critical point for divergence in this paper. By doing so, it was found that the critical flow velocity for divergence is $\mathcal{U}_{\mathrm{BP}}^{(1)} = 6.5$, as shown in figure 6*a*.

Figure 6*b* shows the experimental (the asterisks) and theoretical (heavy solid line) bifurcation diagrams, for the whole range of attainable flow velocities in the water tunnel. Theoretically, the deflection should be zero, from $\mathcal{U} = 0$ to the critical flow velocity for divergence, $\mathcal{U}_{\mathrm{BP}}$, when the amplitude should increase precipitously with flow. In the experiments, however, one obtains non-zero η for all $0 < \mathcal{U} < \mathcal{U}_{\mathrm{BP}}$, as seen in figure 6*b* for the experimental results. In what we refer to as the first zone in the experimental bifurcation diagram, non-zero deflection amplitudes are observed due to the growth of initial geometric and structural imperfections of the cylinder. The second zone is for $\mathcal{U} > \mathcal{U}_{\mathrm{BP}}$ where η increases much more rapidly with $\mathcal{U}$, showing the occurrence of divergence. To find the critical flow for divergence, one can fit the results in the two above-mentioned zones by two straight lines and consider the flow velocity at their intersection as the critical flow for divergence (see figure 6*b*). We call this 'the second method'

[2] Although the deformation was sensed at the midpoint of the cylinder, the second mode was still picked up, since, with flow, the midpoint is not a stationary node.

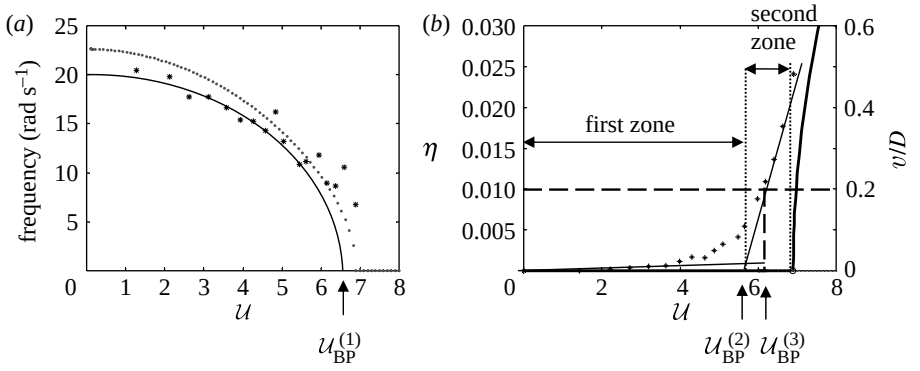

Figure 6. (*a*) Experimental (asterisk) and theoretical (dot) graphs of frequency versus dimensionless flow velocity for a typical series 1 experiment; the continuous line is the parabola fitted to the experimental results. (*b*) Theoretical (heavy continuous line) and experimental (asterisk) bifurcation diagrams.

Table 3. The experimental critical flow velocities for the onset of divergence based on the three methods discussed in §4, together with the corresponding theoretical result for the clamped–sliding cylinder of the first series of experiments with physical parameters given in table 1 and the corresponding error.

	first method, $\mathcal{U}_{\mathrm{BP}}^{(1)}$	second method, $\mathcal{U}_{\mathrm{BP}}^{(2)}$	third method, $\mathcal{U}_{\mathrm{BP}}^{(3)}$	theory, $\mathcal{U}_{\mathrm{BP}}^{\mathrm{th}}$
values	6.5	5.8	6.2	6.9
error (%)	5.8	15.9	10.1	—

for determining the critical flow velocity for divergence. In this case, the critical flow velocity for divergence is $\mathcal{U}_{\mathrm{BP}}^{(2)} = 5.8$, as shown in figure 6*b*.

Another, pragmatic criterion used to define the critical value for divergence is to define its threshold at $\eta = 0.01$ or $v/D = 0.2$. If the cylinder amplitude exceeds this threshold, the cylinder may be considered buckled. This is 'the third method' for determining the critical flow velocity for divergence in this paper, and it yields $\mathcal{U}_{\mathrm{BP}}^{(3)} = 6.2$ for this system (see figure 6*b*).

Table 3 lists the critical values for divergence found by the three methods discussed above, together with the corresponding theoretical value. The first method is in very good agreement with the theoretical result, with only 5.8% error; this does not necessarily mean, however, that this method is superior to, say, the second.

For the theoretical results, the non-dimensional parameters given in table 2 have been used, where Π_0, β, γ, h, χ and ε are calculated using the physical parameters of the cylinder given in table 1.[3] The coefficient of transverse form drag, c_{d}, can also be calculated, following Païdoussis (2004, appendix Q)[4]:

[3] $h = D/D_{\mathrm{ch}}$ and $\chi = \left(D_{\mathrm{ch}}^2 + D^2\right)/\left(D_{\mathrm{ch}}^2 - D^2\right)$, according to Païdoussis (2004, p. 796).

[4] In Païdoussis (2004, appendix Q), the following relation is given: $c_{\mathrm{d}}^{\mathrm{lin}} = (4/\pi)(\mathcal{U}/U)C_{\mathrm{D}}$, where $C_{\mathrm{D}} = (\pi/2)D\Omega C_{\mathrm{d}}$ and $C_{\mathrm{d}} = 2\sqrt{2}/\sqrt{S}$, in which $S = \Omega R^2/\nu$. Now, substituting these relations backwards, one finds $C_{\mathrm{d}} = 4\sqrt{2}/D\sqrt{\Omega/\nu}$, and therefore $C_{\mathrm{D}} = 2\pi\sqrt{2\Omega\nu}$; assuming further that $\mathcal{U}/U \simeq O(1)$, one obtains $c_{\mathrm{d}}^{\mathrm{lin}} = 8\sqrt{2\Omega\nu}$. It can be shown that the coefficient used in nonlinear calculations is $c_{\mathrm{d}} = c_{\mathrm{d}}^{\mathrm{nonlin}} = c_{\mathrm{d}}^{\mathrm{lin}}/\Omega = 8\sqrt{2\nu/\Omega}$.

$c_d = 8\sqrt{2\nu/\Omega}$, where Ω is the radian frequency and ν the kinematic viscosity; for water flow, $\nu = 10^{-6}\ \mathrm{m^2\ s^{-1}}$. One can take $c_n/c_t = 1$ and the tangential frictional coefficient to be $c_t = 0.025$. The effect of the frictional terms on the threshold of divergence is small, and using different values of c_n and c_t has little effect on the theoretical results. However, as discussed in §6, this is not the case for dynamic instabilities.

5. Second series of experiments: clamped–clamped cylinder with no sliding

In this series of experiments, the same cylinder, clamped at both ends was used, but no end-sliding was permitted. Similarly to the first series of experiments, the midpoint displacement of the cylinder was measured at each flow velocity and the corresponding PSD plots were produced. The dominant frequency, e.g. at $f_1 = 3$ Hz for $\mathcal{U} = 3.2$, can be identified with the first eigenfrequency of the system. The PSD plot at, for example, $\mathcal{U} = 6.1$ shows three peaks: at $f_1 = 2$ Hz, $f_2 = 8$ Hz and $f_3 = 17$ Hz (not shown here), which correspond to the first, second and third eigenfrequencies of the buckled system, respectively; it is noted that the dominant first-mode frequency peak has migrated further towards zero vis-à-vis its value at zero flow, but it is not zero. In this regard, it is noted that, in contrast to linear theory, nonlinear theory does not imply zero net rigidity in the buckled state, and the first, second and third mode frequencies are those of the buckled cylinder.

Figure 7*a*,*b* is of the same nature as figure 6*a*,*b*. For $\mathcal{U} < 5$, the experimental values for the frequency of vibrations follow the theoretical curve very closely. For higher flow velocities, however, the experimental values deviate from the theoretical ones and it seems that they tend towards a constant value: $\omega_1 = 10\ \mathrm{rad\ s^{-1}}$, in contrast to the theoretical curve, which goes towards zero parabolically. This deviation is due to the fact that, in the experiments, because axial sliding is prevented, increased deflection generates an increase in tension and therefore the frequency never approaches zero (figure 7*b* shows the non-zero pre-buckling deflection of the cylinder). The theory, on the other hand, assumes that there is no pre-buckling transverse deflection, and therefore that there is no tension in the cylinder before the onset of buckling. It ought to be noted that, in fitting the parabola to estimate the critical flow velocity for divergence by the first method, only the sampling points which follow a parabolic trend have been taken into account and the almost-constant-frequency points have been neglected. The fitted parabola shown in figure 7*a* yields the corresponding critical flow velocity $\mathcal{U}_{\mathrm{BP}}^{(1)} \simeq 6.8$.

In figure 7*b*, it is seen that the post-buckling range in the bifurcation diagram is very limited ($6.3 < \mathcal{U} < 7$), making it difficult to reach any major conclusions as to the post-buckling behaviour of the system. However, for the available range, the experimental amplitude of buckling is in good agreement with the theoretical one. The first row in table 4 gives the critical values for the pitchfork bifurcation found using the three methods previously discussed, together with the corresponding theoretical result. Reasonably good agreement is obtained between the theory and the experiment.

Because, in both cases discussed so far, divergence occurred at a flow velocity very close to the maximum flow attainable in the water tunnel, it was not possible to study the post-divergence behaviour of the system. In what follows,

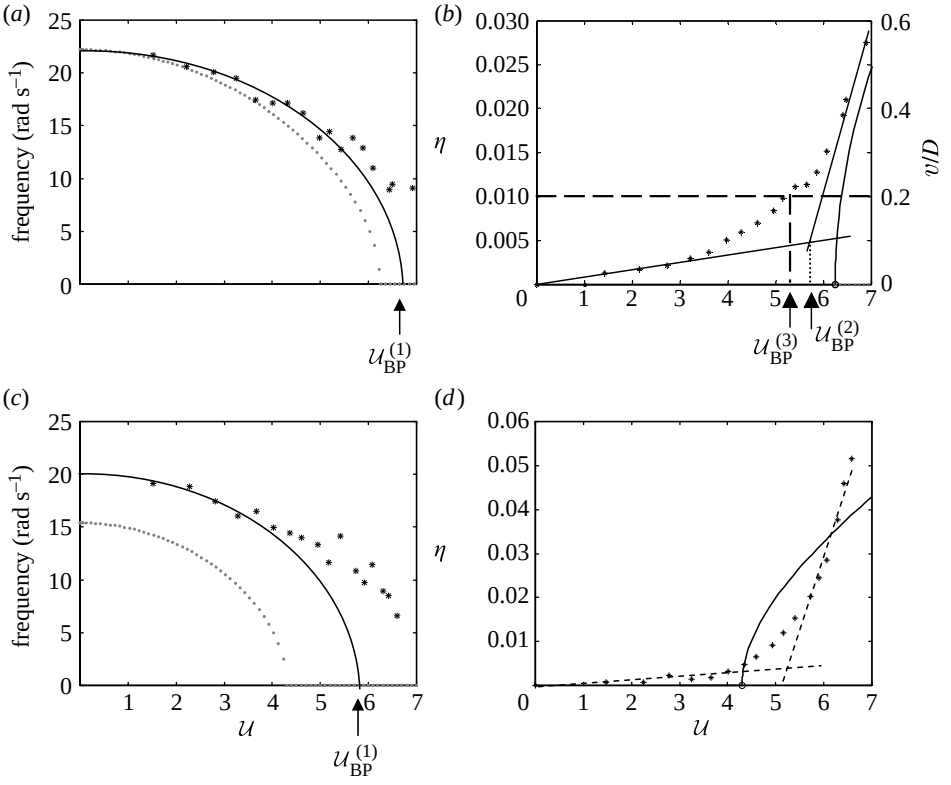

Figure 7. Experimental and theoretical results for the second series of experiments with a clamped–clamped cylinder with no end-sliding and with parameters given in table 1. (*a*) Experimental (asterisk) and theoretical (dot) graphs of frequency versus dimensionless flow velocity for a typical series 2 experiment; (*b*) comparison between theory (continuous line) and experiment (asterisk) in the form of bifurcation diagrams; (*c*,*d*) same graphs for the cylinder under an externally applied axial compression of $\bar{\Gamma} = -20.6$.

we discuss the experiments with the same cylinder under axial compression; in this case, the critical non-dimensional flow velocity for divergence is lower than that in the present case, making it possible to observe the post-divergence behaviour of the cylinder over a wider flow range.

To apply an axial compression to the cylinder, rings of varying thickness, with the same outer diameter as the cylinder ($D_{\mathrm{r,o}} = D = 0.0254$ m) and with the inner diameter of $D_{\mathrm{r,i}} = 0.0067$ m were inserted between the lower end of the cylinder and the lower support assembly (see figure 2*b*). The inserted ring, depending on its thickness, results in pre-straining (shortening) the cylinder and therefore applies a pre-stress (an axial compression) on the cylinder with no flow.

To relate the applied axial pre-straining to the non-dimensional compression, $-\bar{\Gamma}$, we start from the definition $\bar{\Gamma} = \bar{T}L^2/EI$, where $\bar{T} = \sigma A = E\varepsilon A$. Therefore, $\bar{\Gamma} = \Delta AL/I$, where Δ is the pre-shortening and A is the cylinder cross-sectional area. The other quantities are defined in table 1. Therefore, $\bar{\Gamma} = 1.29 \times 10^4\, \Delta$, where it is understood that in these experiments Δ and $\bar{\Gamma}$ are negative.

The procedure, measurements and the nomenclature of the figures are the same as previously described. Three different values for axial compression were

Table 4. The experimental critical flow velocities for the onset of divergence based on the three methods discussed in the text, together with the corresponding theoretical results for the second series of experiments, for the clamped–clamped cylinder with the physical parameters as in table 1, for different values of externally applied axial compression.

		critical value of $\mathcal{U}_{\mathrm{BP}}(-)$			
		experiment			
pre-shortening (mm)	axial compression $-\bar{\Gamma}$	first method	second method	third method	theory
0.0	0	6.8	5.8	5.3	6.25
1.0	12.9	6.1	5.5	5.0	5.12
1.6	20.6	5.8	5.4	5.0	4.30
2.3	29.7	5.3	4.2	4.5	3.10

used in the experiments, namely $\bar{\Gamma} = -12.9$, -20.6 and -29.7. The graphs of the frequency of turbulence-induced vibrations of the cylinder versus the flow velocity were produced for each case. Figure 7*c* shows the graph for an axial compression of $\bar{\Gamma} = -20.6$ as an example (the other cases are not shown). In all these cases, similarly to the case of no axial compression, from a certain flow velocity on, the frequencies do not follow the theoretical parabola; they tend to an almost constant asymptote, instead of continuing towards zero. By increasing the axial compression, the deviation of the experimental results from the theoretical curve starts at lower flow velocities, due to the fact that the original position of the cylinder in the experiment, even before turning on the flow, was not totally straight anymore, as a result of the relatively large applied initial compression. A non-negligible bow existed at zero flow, which is not taken into account in the theory; the theory presumes an initially straight cylinder.[5] This deviation from the theoretical assumptions affects the pre-buckling behaviour of the system much more than the post-buckling behaviour. The reason is that the theory assumes a straight cylinder, while in the experiment the cylinder is not straight before buckling. After buckling, the cylinder is no longer straight in both theory and experiment.

The bifurcation diagrams for the system under axial compression were also produced for all these cases (see figure 7*d* for an example). As the axial compression increases, the range of flow velocity in which the cylinder is buckled becomes wider and, therefore, the amplitude of buckling can be compared more meaningfully with the theoretical results. Fairly good quantitative agreement between theory and experiment is observed in figure 7*d*. Similarly to the case of a clamped–sliding or clamped–clamped cylinder with no end-sliding and no axial compression, the main qualitative difference is that in the experimental results the amplitude of the buckled cylinder increases with flow exponentially, while theory predicts a parabolic increase in the amplitude. The imperfections and the deformation-induced tension in the cylinder can be thought of as the main source for the difference.

[5] The occurrence of the bow of course means that the cylinder has developed buckling due to compression a great deal sooner (for smaller compression) than theoretically predicted, because of imperfections.

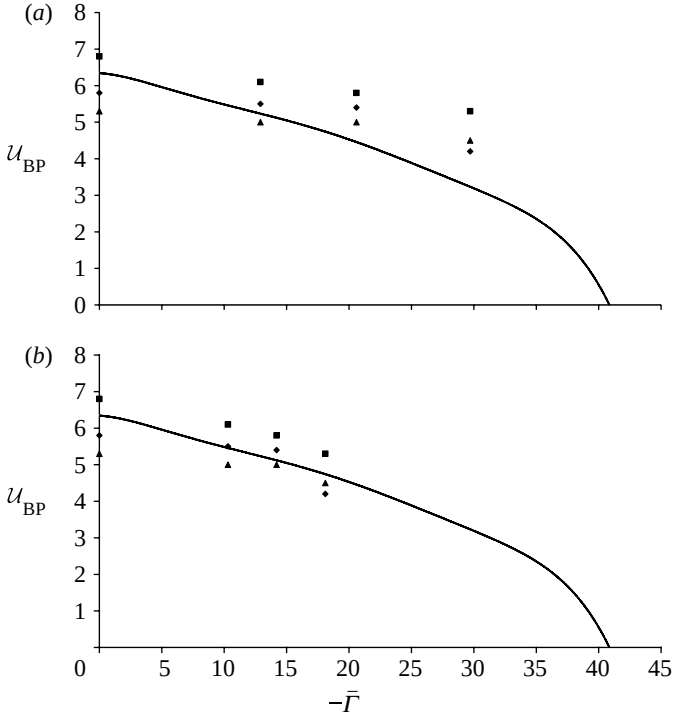

Figure 8. Critical flow velocities for divergence of the cylinder clamped at both ends and with no end-sliding (series 2 experiments with parameters given in table 1) for different externally applied axial compressions, found by using the three methods discussed in the paper, assuming the cylinder is initially (*a*) straight and (*b*) bowed. The continuous line is the corresponding theoretical curve. Filled squares, first method; filled triangles, second method; filled diamonds, third method.

The critical flow velocities for divergence are given in table 4. They are also plotted in figure 8*a* and compared with theory. The theoretical result (continuous line) shows that, as expected, by increasing the axial compression, the critical flow velocity for divergence decreases, and at a certain value of axial compression the cylinder buckles even with no flow. This occurs at $-\bar{\Gamma} \simeq 41$, which is slightly different from the critical value of the Euler problem for a clamped–clamped column, $-\bar{\Gamma} = 4\pi^2$, due to the effect of gravity, which increases the critical value for divergence. It is noted that, as the axial compression becomes larger, agreement of experiment with theory deteriorates. The main reason for this is that, owing to imperfections, the cylinder bows away from the straight configuration; and, in doing so, releases some of the compression that would have otherwise been present, had it remained straight. Thus, the actual value of $-\bar{\Gamma}$ to which the cylinder is subjected at the beginning of the experiment (for $\mathcal{U} = 0$) is lower than theoretically calculated; meaning that for high enough values of $-\bar{\Gamma}$ the experimental points should really be moved to the left, thus closer to the theoretical prediction. This, indeed, is what happens, as shown in figure 8*b*.

In figure 8*b*, the 'effective' values of $-\bar{\Gamma}$, $-\bar{\Gamma}_{\mathrm{eff}}$, were calculated by a simple model, taking into account the reduction in compression as outlined above, assuming the maximum amplitude due to imperfection-related bowing to be

10 mm and a half-sinusoid for the bowed cylinder at $\mathcal{U}=0$; then, the bowed cylinder length is calculated, and the effective (reduced) value of the ring thickness calculated, based on which $-\bar{\Gamma}_{\mathrm{eff}}$ may be deduced from the original $-\bar{\Gamma}$. As seen in figure 8*b*, the experimental results are felicitously closer to theory than they are if this compression relief is not accounted for.

For all the cases studied in this series of experiments, the cylinder did not undergo any dynamic instability before the maximum attainable flow velocity was reached, encouraging us to conduct another series of experiments with a more flexible clamped–clamped cylinder, as discussed in §6, in order to hopefully observe the post-divergence dynamic instability predicted by theory.

6. Third series of experiments: a more flexible cylinder with no end-sliding

In this series of experiments a more slender, hollow flexible clamped–clamped cylinder was used. The same set-up as for the previous series of experiments was used.

Similarly to the previous experiments, at small flow velocities the cylinder was straight and the turbulence-induced vibrations were damped (figure 9*a*). With increasing flow, the cylinder buckled essentially in a first beam-mode shape (figure 9*b*) and the amplitude of buckling increased with flow (figure 9*c*). When the flow reached almost the maximum possible, the cylinder started to oscillate in its second mode around its equilibrium position (figure 9*d*). This is also shown in the electronic supplementary material video. In what follows, the observations are discussed quantitatively.

Figure 10*a* shows how the frequency of turbulence-induced vibrations varies with the non-dimensional flow velocity. Comments similar to those made for the other experiments can be made here also. The critical flow velocity for divergence based on this graph is $\mathcal{U}_{\mathrm{BP}}^{(1)} \simeq 7.5$, which is larger than the theoretical value of $\mathcal{U}_{\mathrm{BP}}^{\mathrm{th}} = 6.25$. Figure 10*b* shows the bifurcation diagram of the system. For small flow velocities, the cylinder behaviour is similar to that previously discussed, in the sense that there is a sharp increase in the rate of change of cylinder deflection amplitude with flow, corresponding to the onset of divergence. The critical flow velocity for divergence is at $\mathcal{U}_{\mathrm{BP}}^{(3)} \simeq 6.2$ by the third method; and at $\mathcal{U}_{\mathrm{BP}}^{(2)} \simeq 5.4$ by the second method. The cylinder buckles mainly in its first mode and the amplitude of buckling increases with flow until $\mathcal{U} \simeq 10$, where a sudden decrease in the experimental midpoint deflection amplitude of the cylinder is observed for a short range of flow, after which the cylinder begins to oscillate, mainly in its second mode, at $\mathcal{U} \simeq 11.2$. As seen in figure 10*b*, the oscillatory motion occurs just before the maximum available flow is attained ($\mathcal{U}_{\max} \simeq 11.5$).

Figure 11*a–c* shows the PSD plots of this cylinder in the pre-buckling ($\mathcal{U}=4.2$), buckled ($\mathcal{U}=6.5$) and oscillatory ($\mathcal{U}=11.2$) states. The three peaks in the PSD plot for $\mathcal{U}=4.2$ ($f_1=3$, $f_2=8$ and $f_3=16$) may be identified with the first, second and third eigenfrequencies of the system. With increasing flow, the peaks move to the left; at $\mathcal{U}=6.5$, they are at $f_1=2$, $f_2=7$ and $f_3=15$. The two peaks in the PSD plot for $\mathcal{U}=11.2$ most probably correspond to the second and the third eigenfrequencies of the system (at $f=1.8$ and 3.3), the first mode being the small peak at $f=0.8$. This ties in with the fact that the observed oscillations were of predominantly second-mode shape, with a sizable third-mode

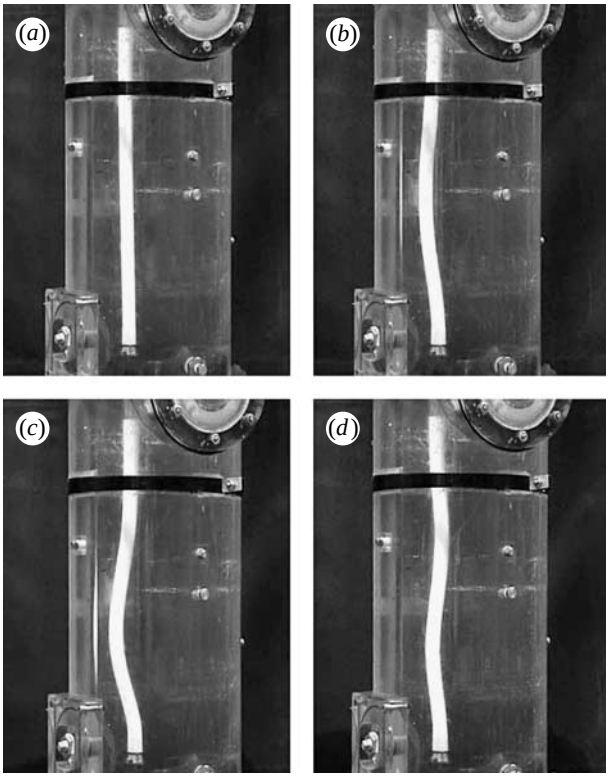

Figure 9. The cylinder of the third series of experiments at different states: (*a*) pre-buckling, (*b*) small-amplitude buckling, (*c*) large-amplitude buckling and (*d*) oscillatory motions.

contribution. Figure 11*d* shows the time history of the oscillatory motion of the cylinder at $\mathcal{U}_{\mathrm{HB}}^{\mathrm{exp}} = 11.2$, where the displacement measured by the first measuring device is plotted for a time interval of 10 s.

The parameters used in the theoretical calculations to compare the results with the experimental observations are given in table 2, corresponding the quantities given in table 1 (series 3). Some of the parameters, however, cannot be determined with certainty, namely those related to the viscous terms (namely c_{n}, c_{t} and c_{d}). These parameters related to the damping and viscous forces can vary over a certain range, depending on the cylinder and character of the flow. The influence of these parameters on the critical flow velocity for the Hopf bifurcation has been carefully studied theoretically. It was found that their effect on the threshold of post-divergence flutter of this system (which is inherently conservative, bar the dissipative and viscosity-related frictional effects) is quite substantial,[6] unlike for the inherently non-conservative

[6] For instance, one would suspect that c_{d} would have an important effect, and it does: varying c_{d} from zero to 0.08 changes $\mathcal{U}_{\mathrm{HB}}$ from 21.8 to 35.5 approximately (with the other parameters as in table 3). On the other hand, for $c_{\mathrm{n}} = c_{\mathrm{t}}$, the effect of varying the two together is rather smaller. But, if $c_{\mathrm{n}} \neq c_{\mathrm{t}}$, their ratio $c_{\mathrm{n}}/c_{\mathrm{t}}$ has an 'unexpectedly' important effect: $8.5 < \mathcal{U}_{\mathrm{HB}} < 27$ for $0.5 < c_{\mathrm{n}}/c_{\mathrm{t}} < 2$, where $c_{\mathrm{n}}/c_{\mathrm{t}} = 0.5$ for rough cylinders and $c_{\mathrm{n}}/c_{\mathrm{t}} = 2$ for smooth ones (Ortloff & Ives 1969); in the light of fluid–structure energy-transfer considerations, however, this is hardly surprising (refer to Païdoussis (2004, §8.3.3)).

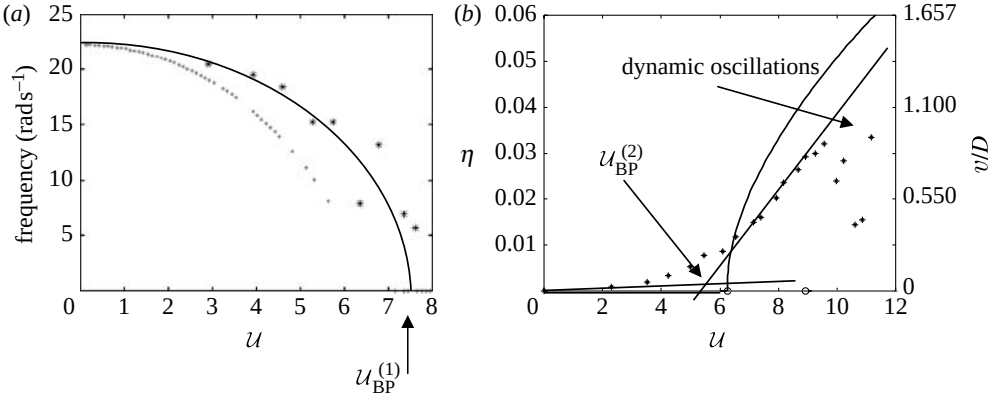

Figure 10. Comparison between theory and experiment for the third series of experiments with a small-diameter clamped–clamped cylinder with no end-sliding and with the parameters given in table 1. (*a*) Experimental (asterisk) and theoretical (dot) graphs of frequency versus dimensionless flow velocity; (*b*) comparison between theory (continuous line) and experiment (asterisk) in the form of bifurcation diagrams.

system of a cantilevered cylinder in axial flow, for instance. Taking the reasonable values of $c_t = 0.02$, $c_n/c_t = 0.5$ (the cylinder is hydrodynamically rough), $c_d = 0.005$ (see Païdoussis (2004, appendix Q)) and taking into account structural damping ($\alpha^u = \alpha^v = 1$) (see Modarres-Sadeghi 2006), the theoretical critical flow velocity for the Hopf bifurcation is found to be $U_{HB}^{th} = 15.7$, which is quite different, but not unreasonably far from the experimental value of 11.2.

According to the theoretical results, the cylinder oscillates around its buckled state and the frequency of oscillation is $f^{th} = 3$ Hz; in the experiments, on the other hand, the cylinder oscillates around its original equilibrium position (inexplicably, as predicted by *linear* theory) with a frequency of $f^{exp} = 1.8$ Hz.[7] These two frequencies are of comparable magnitude. The difference in the nature of oscillations (around the buckled state in theory and around the original equilibrium position in experiment) could be due to the fact that the model used for the theoretical predictions is correct to third-order magnitude; perhaps, to capture the relatively large-amplitude oscillations of the system, one needs to use a higher-order model (e.g. fifth order).

To study the influence of the externally applied axial compression on the dynamic instability of the system, experiments were conducted with this small-diameter cylinder, with a ring inserted between the lower end of the cylinder and the downstream support, applying an axial compression of $\bar{T} = -19.0$. Similarly to the case of the large-diameter cylinder (§5), under axial compression the cylinder buckles at a lower flow velocity, and the amplitude of buckling at a given flow velocity is larger than that of the cylinder with no axial compression. The critical flow velocities for divergence obtained by the three methods discussed before are $U_{BP}^{(1)} = 6.1$, $U_{BP}^{(2)} = 5.0$, $U_{BP}^{(3)} = 4.3$, while

[7] It is recalled that linear theory predicts that the onset of flutter arises by the locus emerging from the imaginary-frequency axis in Argand diagrams, with essentially zero frequency; the frequency increases thereafter as the flow velocity is increased.

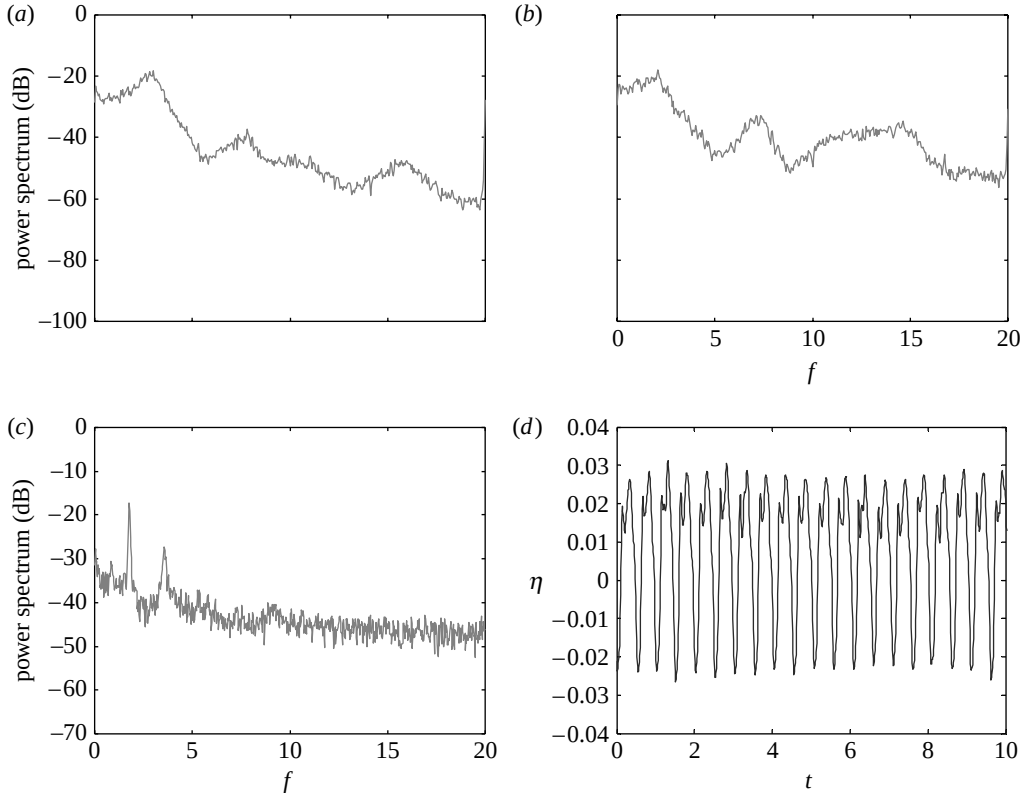

Figure 11. PSD plots for the third series of experiments with a small-diameter clamped–clamped cylinder with no end-sliding and with the parameters given in table 1 at (*a*) $\mathcal{U}=4.2$, (*b*) $\mathcal{U}=6.5$ and (*c*) $\mathcal{U}=11.2$, together with (*d*) the time history at $\mathcal{U}=11.2$.

$\mathcal{U}_{\mathrm{BP}}^{\mathrm{th}}=4.5$; thus, except for the first method, reasonably good agreement between the theoretical and experimental values is obtained. What is remarkable in this case is that flutter occurs at almost the same flow velocity as with no axial compression! In fact, the cylinder under axial compression buckles at a lower flow velocity ($\mathcal{U}\simeq 4.5$), and remains buckled for a wider range of flow velocities, until it starts oscillating at $\mathcal{U}\simeq 11$. This is in agreement with what the theoretical nonlinear model predicts. The theoretical value for $\bar{\Gamma}=-19$ is approximately the same as for $\bar{\Gamma}=0$ ($\mathcal{U}_{\mathrm{HB}}\simeq 15.7$).[8] By changing the external axial compression from 0 to -150, the critical flow velocity for the Hopf bifurcation increases smoothly from $\mathcal{U}=21.8$ to 22.3. The change in the critical flow for varying $\bar{\Gamma}$ from 0 to -19 is almost negligible according to these results. Also, looking at the nonlinear equations of motion of the system (Modarres-Sadeghi *et al.* 2005), one can see that all the terms involving $\bar{\Gamma}$ (the non-dimensional axial tension/compression parameter) are associated with static terms, i.e. terms with no time derivatives of the unknowns. This, however, does not imply that there should be no effect, or a negligible effect, on the dynamic behaviour of the system as $\bar{\Gamma}$ is varied.

[8] Indeed, changing $\bar{\Gamma}$ from zero to -150 produces a change in $\mathcal{U}_{\mathrm{HB}}$ of the order of 5% only.

7. Conclusions

Three series of experiments have been conducted to study the dynamical behaviour of slender flexible cylinders clamped at both ends and subjected to axial flow. The downstream end of the cylinder could either slide axially or was wholly fixed.

Nonlinear theory predicts that the system loses stability via a pitchfork bifurcation, leading to buckling, and that at higher flows a Hopf bifurcation occurs, emanating from the statically divergent solution. The second mode of the system becomes unstable at the Hopf bifurcation and the cylinder oscillates about the buckled state. This periodic oscillation is then followed by quasi-periodic and chaotic ones. The existence of the post-divergence dynamic instability had previously been predicted by Païdoussis (1966*a*, 1973) using a linear model and was confirmed by experiments (Païdoussis 1966*b*), but the interest in those experiments was confined to the linear realm.

Here, in the first series of experiments, the lower end of the cylinder was free to slide axially, while in the second series, axial sliding was prevented. In all the experiments, small static deflections were observed at small flow velocities, reflecting the growth of the initial material and geometric imperfections. After a certain flow velocity, the cylinder amplitude increased more rapidly with flow. This flow velocity corresponds to the critical value for divergence. When applying axial compression in the case of fixed ends, it was observed that the critical flow velocity for divergence decreased, while for a given flow velocity, the amplitude of buckling increased, as one would expect. Good agreement between theoretical and experimental results was observed for both the critical flow velocity for divergence and the amplitude of buckling. No dynamic instabilities were observed in these two series of experiments because the cylinder was rather stiff, hence the maximum attainable dimensionless flow velocity was insufficiently high for that.

The third series of experiments were conducted with a more flexible hollow cylinder, making it possible to reach higher dimensionless flow velocities. Similarly to the previous two series of experiments, the cylinder buckled, and the amplitude of buckling increased with flow. In this case, however, at higher flow, the cylinder developed a dynamic instability (flutter) and oscillated mainly in its second mode. This proves, experimentally, the existence of post-divergence flutter, previously predicted by linear theory and the nonlinear theoretical model. These observations also confirm the experimental results of Païdoussis (1966*b*). It was observed that the theoretical value for the Hopf bifurcation was largely dependent on the dissipation- and fluid friction-related system parameters, for which (to the best available knowledge) precise values cannot be assigned. However, based on a separate theoretical parametric study on the effect of these parameters on the flutter threshold, and using reasonable values, experimental flutter thresholds were found to be within 30% of the theoretical values. This is not satisfactorily close, indicating that further work needs to be done in this respect. It was also observed, both experimentally and theoretically, that the influence of externally applied axial compression on the onset of post-divergence flutter is negligible for the range of parameters of this study.

The authors gratefully acknowledge the support given to this research by the Natural Sciences and Engineering Research Council of Canada (NSERC).

Appendix A. Nonlinear equations of motion

The nonlinear equations of motion for the system of a slender cylinder subjected to axial flow have been derived by Modarres-Sadeghi *et al.* (2005) and in their non-dimensional form are

$$
\begin{aligned}
&(1-\beta)\ddot{\zeta}-\chi\Big(\beta\,\ddot{\eta}\eta'+2\,\mathcal{U}\sqrt{\beta}\dot{\eta}'\eta'+\mathcal{U}^2\eta''\eta'\Big)-\Pi_0(\zeta''+\eta'\eta'')-(\eta''\eta'''+\eta'\eta^{(4)})\\
&\quad-\frac{1}{2}\varepsilon\mathcal{U}^2(c_{\mathrm{n}}-c_{\mathrm{t}})\left(\frac{\sqrt{\beta}}{\mathcal{U}}\dot{\eta}\eta'+\eta'^2\right)+\frac{1}{4}\varepsilon c_{\mathrm{t}}\beta\dot{\eta}^2+\frac{1}{2}\varepsilon\mathcal{U}^2c_{\mathrm{t}}(1+h)\\
&\quad\times\left[\zeta'-\frac{\eta'^2}{2}+\left(1-\frac{1}{2}\delta-\xi\right)\eta'\eta''\right]-\frac{1}{2}\varepsilon\mathcal{U}^2c_{\mathrm{d}}\eta'\left(\eta'|\eta'|+\frac{\sqrt{\beta}(\eta'|\dot{\eta}|+\dot{\eta}|\eta'|)}{\mathcal{U}}\right.\\
&\quad\left.+\frac{\beta\dot{\eta}|\dot{\eta}|}{\mathcal{U}^2}\right)+\left[\frac{1}{2}\mathcal{U}^2c_{\mathrm{b}}(1-\delta)+\bar{\Gamma}\delta+(1-2\nu)\bar{\Pi}\delta\right]\eta'\eta''\\
&\quad+\gamma\left[\zeta'-\frac{\eta'^2}{2}+\left(1-\frac{1}{2}\delta-\xi\right)\eta'\eta''\right]+O(\epsilon^5)=0
\end{aligned}
\tag{A 1}
$$

and

$$
\begin{aligned}
&(1+(\chi-1)\beta)\ddot{\eta}+2\chi\mathcal{U}\sqrt{\beta}\dot{\eta}'\left(1-\frac{7}{4}\eta'^2\right)+\chi\mathcal{U}^2\eta''\left(1-\frac{5}{2}\eta'^2\right)-\chi\eta'(\beta\ddot{\zeta}+3\sqrt{\beta}\mathcal{U}\dot{\zeta}'\\
&\quad+2\mathcal{U}^2\zeta'')-\chi\beta\ddot{\eta}\eta'^2-\chi\left(4\mathcal{U}\zeta'+2\sqrt{\beta}\dot{\zeta}+\frac{3}{2}\sqrt{\beta}\dot{\eta}\eta'\right)\left(\sqrt{\beta}\dot{\eta}'+\mathcal{U}\eta''\right)\\
&\quad+\left[\frac{1}{2}\mathcal{U}^2c_{\mathrm{b}}(1-\delta)+\bar{\Gamma}\delta+(1-2\nu)\bar{\Pi}\delta\right]\left(-\eta''+\eta'\zeta''+\eta''\zeta'+\frac{3}{2}\eta'^2\eta''\right)\\
&\quad+\frac{1}{2}\varepsilon\mathcal{U}^2\,c_{\mathrm{d}}\left(\eta'|\eta'|+\frac{\sqrt{\beta}(\eta'|\dot{\eta}|+\dot{\eta}|\eta'|)}{\mathcal{U}}+\frac{\beta\dot{\eta}|\dot{\eta}|}{\mathcal{U}^2}\right)-\Pi_0\left(\zeta''\eta'+\zeta'\eta''+\frac{3}{2}\eta'^2\eta''\right)\\
&\quad+v^{(4)}-(8\eta'\eta''\eta'''+\eta'\zeta^{(4)}+2\eta'^2\eta^{(4)}+2\eta''^3+2\zeta'\eta^{(4)}+4\zeta''\eta'''+3\zeta'''\eta'')\\
&\quad+\frac{1}{2}\varepsilon\mathcal{U}^2c_{\mathrm{t}}(1+h)\left(-\frac{1}{2}\eta'^3+[\zeta-\zeta(1)(1-\delta)]\eta''+\left(1-\frac{1}{2}\delta-\xi\right)\right.\\
&\quad\left.\times\left(-\eta''+\eta'\zeta''+\eta''\zeta'+\frac{3}{2}\eta'^2\eta''\right)\right)-\frac{1}{2}\varepsilon\mathcal{U}^2(c_{\mathrm{n}}-c_{\mathrm{t}})\left(\eta'^3+\eta'\zeta'+\beta\frac{\dot{\eta}\eta'^2}{\mathcal{U}}+\frac{1}{2}\beta\frac{\dot{\eta}^2\eta'}{\mathcal{U}^2}\right)\\
&\quad+\frac{1}{2}\varepsilon\mathcal{U}^2(c_{\mathrm{n}}+c_{\mathrm{t}}h)\eta'+\frac{1}{2}\varepsilon\mathcal{U}^2c_{\mathrm{n}}\left(\frac{\sqrt{\beta}}{\mathcal{U}}\dot{\eta}+\frac{\sqrt{\beta}}{\mathcal{U}}\zeta'\dot{\eta}+\frac{\beta}{\mathcal{U}^2}\dot{\zeta}\,\dot{\eta}-\frac{1}{2}\frac{\beta^{3/2}}{\mathcal{U}^3}\dot{\eta}^3\right)\\
&\quad+\gamma\left\{\eta'-\frac{1}{2}\eta'^3+[\zeta-\zeta(1)(1-\delta)]\eta''+\left(1-\frac{1}{2}\delta-\xi\right)\right.\\
&\quad\left.\times\left(-\eta''+\eta'\zeta''+\eta''\zeta'+\frac{3}{2}\eta'^2\eta''\right)\right\}+O(\epsilon^5)=0,
\end{aligned}
\tag{A 2}
$$

where the non-dimensional parameters are related to the dimensional ones using the following relations:

$$\xi = \frac{X}{L},\quad \zeta = \frac{u}{L},\quad \eta = \frac{v}{L},\quad \tau = \left(\frac{EI}{m+\rho A}\right)^{1/2}\frac{t}{L^2},\quad \mathcal{U} = \left(\frac{\rho A}{EI}\right)^{1/2} UL,\quad \beta = \frac{\rho A}{m+\rho A},$$
$$\gamma = \frac{(m-\rho A)gL^3}{EI},\quad c_\mathrm{n} = \frac{4}{\pi}C_\mathrm{N},\quad c_\mathrm{t} = \frac{4}{\pi}C_\mathrm{T},\quad c_\mathrm{d} = \frac{4}{\pi}C_\mathrm{Dp},\quad c_\mathrm{b} = \frac{4}{\pi}C_\mathrm{b},\quad \varepsilon = \frac{L}{D},$$
$$h = \frac{D}{D_\mathrm{h}},\quad \bar{\Pi} = \frac{\bar{P}AL^2}{EI},\quad \bar{\Gamma} = \frac{\bar{T}L^2}{EI},\quad \Pi_0 = \frac{EAL^2}{EI},\quad \chi = \frac{M}{\rho A}. \tag{A 3}$$

In equation (A 3), u and v are displacements in x- and y-directions, respectively; L and D are the cylinder length and diameter; C_b and C_Dp are base and form drag coefficients; C_N and C_T are frictional coefficients in the normal and tangential directions, respectively; EI is the flexural rigidity of the cylinder; ρA is the added mass of the fluid per unit length; m is the mass per unit length of the cylinder; and $\bar{T}$ and $\bar{P}$ are externally applied tension and pressurization, respectively.

References

Chen, S. S. 1987 *Flow-induced vibration of circular structures*. Washington, DC: Hemisphere.

Chen, S. S. & Wambsganss, M. W. 1972 Parallel-flow induced vibration of fuel rods. *Nucl. Eng. Design* **18**, 253–278. (doi:10.1016/0029-5493(72)90144-6)

Doedel, E. J. & Kernéves, J. P. 1986 *Auto: software for continuation and bifurcation problems in ordinary differential equations. Applied mathematics report*. Pasadena, CA: California Institute of Technology. (Procurable from doedel@cs.concordia.ca.)

Dowling, A. P. 1988*a* The dynamics of the towed flexible cylinders. Part 1: neutrally buoyant elements. *J. Fluid Mech.* **187**, 507–532. (doi:10.1017/S0022112088000540)

Dowling, A. P. 1988*b* The dynamics of the towed flexible cylinders. Part 2: negatively buoyant elements. *J. Fluid Mech.* **187**, 533–571. (doi:10.1017/S0022112088000552)

Hawthorne, W. R. 1961 The early development of the Dracone flexible barge. *Proc. Inst. Mech. Eng.* **175**, 52–83.

Kennedy, R. M. 1987 Forced vibration of a thin flexible cylinder in viscous flow. *J. Sound Vib.* **115**, 189–201. (doi:10.1016/0022-460X(87)90465-2)

Lee, T. S. 1981 Stability analysis of the Ortloff–Ives equation. *J. Fluid Mech.* **110**, 293–295. (doi:10.1017/S002211208100075X)

Lopes, J. L., Païdoussis, M. P. & Semler, C. 2002 Linear and nonlinear dynamics of cantilevered cylinders in axial flow. Part 2: the equation of motion. *J. Fluids Struct.* **16**, 715–737. (doi:10.1006/jfls.2002.0448)

Modarres-Sadeghi, Y. 2006 Nonlinear dynamics of slender flexible cylinders subjected to axial flow. PhD thesis, McGill University.

Modarres-Sadeghi, Y., Païdoussis, M. P. & Semler, C. 2005 A nonlinear model for an extensible slender cylinder subjected to axial flow. *J. Fluids Struct.* **21**, 609–627. (doi:10.1016/j.jfluidstructs.2005.02.012)

Modarres-Sadeghi, Y., Païdoussis, M. P. & Semler, C. 2007 The nonlinear behaviour of a slender flexible cylinder pinned or clamped at both ends and subjected to axial flow. *Comput. Struct.* **85**, 1121–1133. (doi:10.1016/j.compstru.2006.08.006)

Ortloff, C. R. & Ives, J. 1969 On dynamic motion of a thin flexible cylinder in a viscous stream. *J. Fluid Mech.* **38**, 713–720. (doi:10.1017/S0022112069002552)

Païdoussis, M. P. 1966*a* Dynamics of flexible slender cylinders in axial flow. Part 1: theory. *J. Fluid Mech.* **26**, 717–736. (doi:10.1017/S0022112066001484)

Païdoussis, M. P. 1966*b* Dynamics of flexible slender cylinders in axial flow. Part 2: experiments. *J. Fluid Mech.* **26**, 737–751. (doi:10.1017/S0022112066001496)

Païdoussis, M. P. 1968 Stability of towed, totally submerged flexible cylinders. *J. Fluid Mech.* **34**, 273–297. (doi:10.1017/S0022112068001898)

Païdoussis, M. P. 1973 Dynamics of cylindrical structures subjected to axial flow. *J. Sound Vib.* **29**, 365–385. (doi:10.1016/S0022-460X(73)80291-3)

Païdoussis, M. P. 1998 *Fluid–structure interactions: slender structures and axial flow*, vol. 1. London, UK: Academic Press.

Païdoussis, M. P. 2004 *Fluid–structure interactions: slender structures and axial flow*, vol. 2. London, UK: Elsevier Academic Press.

Païdoussis, M. P., Grinevich, E., Adamovic, D. & Semler, C. 2002 Linear and nonlinear dynamics of cantilevered cylinders in axial flow. Part 1: physical dynamics. *J. Fluids Struct.* **16**, 691–713. (doi:10.1006/jfls.2002.0447)

Pao, H. P. 1970 Dynamical stability of a towed thin flexible cylinder. *AIAA J. Hydronaut.* **4**, 144–150.

Papanastasiou, T. C., Georgiou, G. C. & Alexandrou, A. N. 2000 *Viscous fluid flow*. Boca Raton, FL: CRC Press.

Poddubny, V. I. & Saltanov, N. V. 1991 Three-dimensional parametric vibrations of filaments or wires in coaxial flows. *Fluid Mech. Sov. Res.* **20**, 33–41.

Poddubny, V. I., Shamarin, J. E., Chernenko, D. A. & Astakhov, L. S. 1995 *Dynamics of undersea towing systems*. St Petersburg, Russia: Sudostroenye.

Sarv, H. & John, J. 2000 Technical and economical aspects of large-scale CO_2 storage in deep oceans. In *Proc. 25th Int. Tech. Conf. on Coal Utilization and Fuel Systems, Clearwater, FL*, vol. 1, paper MTI 00-03.

Semler, C., Gentleman, W. C. & Païdoussis, M. P. 1996 Numerical solutions of second-order implicit ordinary differential equations. *J. Sound Vib.* **195**, 553–574. (doi:10.1006/jsvi.1996.0445)

Semler, C., Lopes, J.-L., Augu, N. & Païdoussis, M. P. 2002 Linear and nonlinear dynamics of cantilevered cylinders in axial flow. Part 3: nonlinear dynamics. *J. Fluids Struct.* **16**, 739–759. (doi:10.1006/jfls.2002.0445)

Sudarsan, K., Bhattacharyya, S. K. & Vendhan, C. P. 1997 An experimental study of hydroelastic instability of flexible towed underwater cylindrical structures. In *Proc. 16th OMAE Conf., Yokohama, Japan*, vol. A, pp. 73–80. New York, NY: ASME.

Sugimoto, S. T. 1996 Aeroelastic stability of a beam traveling in a tunnel lined with resonators. *AIAA J.* **34**, 2005–2013.

Sugimoto, S. T. & Kugo, K. 2001 Wave propagation on an elastic beam traveling in a tube: linear theory of aerodynamic loading. *J. Comput. Acoust.* **9**, 1227–1236. (doi:10.1142/S0218396X01001157)

Tanaka, S., Hirata, T., Kaneko, S. & Watanabe, T. 2001 Aerodynamic vibration of combined rigid bodies due to leakage flow. In *Flow-induced vibration-2001*, vol. 2 (ed. M. J. Pettigrew), pp. 45–52. PVP-Vol. 420-2.

Triantafyllou, G. S. & Chryssostomidis, C. 1984 Analytic determination of the buckling speed of towed slender cylindrical beams. *ASME J. Energy Resources Technol.* **106**, 246–249.

Triantafyllou, G. S. & Chryssostomidis, C. 1985 Stability of a string in axial flow. *ASME J. Energy Resources Technol.* **107**, 421–425.